Available online at www.sciencedirect.com
ScienceDirect
Journal of Catalysis 253 (2008) 200–211
JOURNAL OF CATALYSIS
www.elsevier.com/locate/jcat

# Surface properties of Sr- and Co-doped $LaFeO_3$

John N. Kuhn, Umit S. Ozkan *

*The Ohio State University, Department of Chemical and Biomolecular Engineering, Columbus, OH 43210, USA*

Received 11 June 2007; revised 2 October 2007; accepted 4 October 2007

Available online 14 November 2007

**Abstract**

The surface properties of Fe-based perovskite-type oxides with the formula $La_{0.6}Sr_{0.4}Co_yFe_{1-y}O_{3-\delta}$ for $y = 0.1$, 0.2, and 0.3 were investigated. Using methanol as a probe molecule, the amounts of basic and Lewis surface sites were determined. The types of sites were confirmed using DRIFTS. The surface basicity, as well as the reducibility, oxygen storage capacity, transition metal surface concentration, and methanol oxidation activity, were found to progress through an extrema for the intermediate Co level; that is, the behavior and performance of the samples are nonlinear with respect to increasing Co content. An electronic structural transition is proposed as the explanation for the observed trends.


*Keywords:* Perovskite-type; Solid oxide fuel cell cathode; Surface characterization; Methanol oxidation; Probe molecule; Structure–property relation

## 1. Introduction

Perovskite-type ($ABO_3$) oxide catalysts have been widely researched due to their unique properties which have led to applications in a number of reactions [1–3]. These applications include various total and partial oxidation reactions (e.g., CO, $NH_3$, and organics), hydrogenation, dehydrogenation, hydrogenolysis, photocatalysis, and environmental applications (e.g., $SO_2$ reduction, de-$NO_x$). For methane oxidation, several formulations displayed performance similar to that of Pt on $Al_2O_3$ [2]. In addition to these purely catalytic reactions, perovskite-type materials have been used in several applications in which both their unique surface and bulk properties are exploited. Oxygen separation membranes are a prime example [4,5]. Because only oxygen (as oxide ions) is transported across the dense membranes, high-purity separations of air can be achieved. These devices can be combined with catalytic applications, and oxide ions can be used as the oxidant source for ethane dehydrogenation and oxidative coupling of methane [6,7]. The present work focuses on formulations of interest for solid oxide fuel cell (SOFC) applications.

All four major SOFC components (cathode, electrolyte, anode, and interconnects) are commonly made from perovskite-type oxides [8]. This fact attests to the wide variety of potential behavior of perovskite-type oxides, because the components require very different properties. For example, the electrolyte must be an electronic insulator, and the interconnects must be catalytically inactive, whereas the electrodes must be electronic conductors and have catalytic activity. In particular, perovskite-type oxides are especially important as electrode materials, because cathode alternatives are limited to cermets containing precious metals, such as Pt, and conventional anode materials (Ni-YSZ) deactivate due to sulfur impurities and carbon-based fuels. Whereas Co-based materials were the first proposed perovskite-type oxides as SOFC cathodes, Mn-based materials quickly became popular because of their increased stability under harsh conditions [8]. However, because there was a desire to lower the SOFC operation temperature (mainly achieved by decreasing the thickness of the electrolyte), more active materials were needed at intermediate temperatures (500 to 800 °C). At this range of operating temperatures, materials based on Fe and Co and mixtures thereof are expected to provide improved performance at lower temperatures through increased ionic conduction abilities.

As the ionic conductivity increases, the active reaction area for oxygen reduction expands. When this expansion occurs, the role of interfacial oxygen reduction kinetics becomes increas-

* Corresponding author. Fax: +1 614 292 3769.
*E-mail address:* ozkan.1@osu.edu (U.S. Ozkan).

0021-9517/$ – see front matter 
doi:10.1016/j.jcat.2007.10.005

ingly important. As demonstrated through the work of several researchers, surface processes that are chemical in nature, such as surface oxygen exchange and oxygen surface diffusion, influence the performance of mixed conducting perovskite-type materials [4,9–13]. For SOFC cathodes, Adler has proposed that the performance of mixed conductors is co-limited by ionic diffusion and the activation of molecular gas-phase oxygen. However, despite their newfound importance, few studies have focused on the characterization of the surface of these materials.

The bulk oxygen pathway makes an exclusive study of the surface difficult. For example, oxygen temperature-programmed desorption is truly a bulk technique, because oxygen evolves from the anionic matrix to form oxygen vacancies. During heterogeneously catalyzed reactions, the mechanisms can be intrafacial (involving mobile lattice oxygen) rather than suprafacial (involving adsorbed oxygen). At temperatures high enough for bulk oxygen to become mobile, methane oxidation is an example of an intrafacial reaction [2].

A common surface characterization technique is the use of probe molecules. Whereas simple molecules such as $H_2$, CO, $CO_2$, and $H_2O$ are most common, hydrocarbons also have been used to gain insight into oxidation behavior and evaluate surface acid sites of perovskite-type oxides [2,3,14]. There has been considerable success in using oxygenated hydrocarbons (e.g., alcohols) as probe molecules for supported and bulk oxide materials. Methanol was shown as a useful compound for studying these surfaces. Product formation from methanol surface reactivity was related to the nature of the active sites [15]. Acidic surface sites led to dimethyl ether, whereas redox sites caused formaldehyde production. Basic sites, such as those examined for the perovskite-type oxides in the present study, resulted in the formation of carbon dioxide. Moreover, the ability of a surface to dissociate methanol yields information on the strength of the sites [16,17]. However, such surface studies have not been performed on perovskite-type oxides with stabilities relevant for SOFC cathodes.

Fe-based materials have been the least widely studied of the perovskite-type oxides, because they generally have lower activity than their Co counterparts. For example, studies focusing on the oxidation of propane [18], methanol [18], CO [2], propylene [2], and isobutene [2] have demonstrated that $LaCoO_3$ is more active than $LaFeO_3$. No studies have been performed on Fe-rich $LaFeO_3$ formulations doped with both Sr and Co. Fe-based formulations are desirable because of improved system compatibility, both in terms of lower thermal expansion coefficients (TECs) and lower chemical reactivity with the most common electrolytes (e.g., yttria-stabilized zirconia or YSZ), compared with Co-rich formulations. These materials also may catalyze oxidation reactions; recent work has shown that Fe doping provides structural stability in Co-based materials [19]. Moreover, the addition of Sr into $La(Co,Fe)O_{3-\delta}$ may lead to an activity increase, as was reported for butane oxidation over $(La,Sr)CoO_{3-\delta}$ [20]. On the other hand, an optimal Sr loading was observed for Fe-based materials used for ethanol and propane oxidation [21,22] and Co-based materials used for propane oxidation [18]. When La is doped with divalent cations, catalytic properties (e.g., oxidation activity [23] and oxygen storage capacity [24]) tend to increase with Co content at the expense of stability [19] when Fe and Co are mixed on the transition metal site. However, evidence (maximum methane oxidation activity occurring for $La_{0.8}Sr_{0.2}Fe_{0.6}Co_{0.4}O_{3-\delta}$ compared with pure Co and Fe materials [20]) exists for complex behavior when these transition metals are used simultaneously.

The present work examines the surface properties of $La_{0.6}Sr_{0.4}Co_yFe_{1-y}O_{3-\delta}$ for $y = 0.1$, 0.2, and 0.3. In an extension of the work on simple metal oxides, the surfaces of these mixed perovskite-type oxides were characterized using methanol as a probe molecule. The site density was measured using dynamic chemisorption, whereas the nature of the sites was determined using the products from temperature-programmed desorption (TPD) and *in situ* diffuse reflectance Fourier transform infrared spectroscopy (DRIFTS). Supporting surface information was obtained by X-ray photoelectron spectroscopy (XPS). The results were then used to explain the product distribution and activity differences for the different Co loadings during methanol oxidation.

In a previous study [25], we have reported the bulk characterization of the same materials. According to that work, all samples, due to the doping of Sr, have rhombohedral symmetry and are stoichiometric with respect of oxygen under ambient conditions. At elevated temperatures, the transition to cubic symmetry occurred, and the transition temperature dropped as the Co content increased, as was expected due to size arguments. For the reaction results discussed in this article, however, all three samples are expected to be of rhombohedral symmetry, because the lowest expected transition temperature is near 500 °C. The transition temperature is important because it may lead to significant differences in phase stability under reducing conditions [26,27]. Another important finding from our previous study [25] was that, in contradiction to what is generally perceived for formulations containing Fe and Co, oxygen vacancy formation was not proportional to Co content. This trend occurred under air up to 700 °C and for initial reductions under more reducing environments (e.g., He and 10% $H_2/N_2$). In addition, measured by *in situ* XRD under reducing conditions, the perovskite phase was the only one detected up to 800 °C in the presence of 5% $H_2/N_2$. This result indicates that the perovskite-type phase was the only one present under the reaction conditions used in this study.

## 2. Experimental

The $La_{1-x}Sr_xCo_yFe_{1-y}O_{3-\delta}$ samples were prepared by a conventional solid-state route. The preparation and the BET surface measurements were described previously [25]. The mass specific surface areas of all samples were between 1.5 and 2.0 $m^2/g$.

### 2.1. Dynamic adsorption and temperature-programmed desorption of methanol

Dynamic methanol adsorption and sequential temperature-programmed desorption experiments were performed using a

Thermo-Finnigan Trace Ultra differential scanning quadrupole (DSQ) gas chromatograph/mass spectrometer (GC/MS). Samples (∼150 mg) were loaded into a U-tube shaped quartz reactor between plugs of quartz wool. The samples were exposed to a 30 mL/min flow of 20% $O_2$/He at 850 °C (10 °C/min) with an isothermal hold for 20 min. The samples were cooled to 50 °C under the same flow. At this temperature, the flow was switched to He at 30 mL/min, and the tubing was purged for 1 h. The adsorption was performed at 50 °C to limit physical adsorption and eliminate any combustion. A second He flow (also 30 mL/min) was saturated with methanol in a homemade bubbler at room temperature. The effluent from the bubbler was fed to a 50-μL loop on a 6-port valve (Valco) at 100 °C for the pulsed adsorption. All lines after the bubbler were heated to approximately 100 °C to reduce the methanol adsorption on the walls of the tubing.

The chemisorbed amount was determined by averaging the integrated 15 ($CH_3$), 29 (COH), and 31 ($CH_3O$) $m/z$ fragments. The 32 ($CH_3OH$) $m/z$ signal was not used, because it occasionally displayed spikes caused by the valve switches. The amount of methanol was calculated using the ideal gas and Antoine's equations. The adsorbed amount was calculated assuming that the full pulses correlated with the predicted amount of methanol contained in the loop. The adsorbed amount was converted to site density using the specific surface area assuming 1 site per adsorbed methanol molecule.

Once the signals for methanol related ions reached a steady integrated value, the reactor was purged for 1 h in He. A linear temperature program (50–900 °C at 10 °C/min) was enacted, and the desorption products were monitored. The amount of molecularly adsorbed methanol was determined by evaluating the integrated area for methanol fragments using the full pulses during the adsorption as a response factor. Peak integration was performed with the Grams AI software package.

### 2.2. DRIFTS

*In situ* DRIFTS experiments were performed with a Thermoelectron Nicolet 6700 FTIR spectrometer furnished with a liquid nitrogen-cooled MCT detector and an environmental chamber. Spectra were obtained at a resolution of 4 $cm^{-1}$ using 500 scans between 650 and 4000 $cm^{-1}$. Backgrounds were collected in 25 mL/min of He after a 5-min hold after temperature increases. After the final background was collected, the flow was switched to air (25 mL/min) for 30 min to restore the oxygen content of the sample. The sample was then cooled to 50 °C before the flow was switched back to the He stream, and the chamber was purged for 15 min. The sample was then exposed to a steady stream of methanol (bubbler at room temperature) for 1 h. After a 10-min purge, spectra acquisition began. The temperature was raised in 25 or 50 °C increments, after which the temperature was held constant for 5 min before the scan was enacted.

### 2.3. X-ray photoelectron spectroscopy

X-ray photoelectron spectra (XPS) were collected on a Kratos Ultra Axis Spectrometer using Mg$K_\alpha$ (1253.6 eV) radiation under high vacuum. Samples were ground into carbon tape for analysis. The Mg anode, operated at 13 kV and 10 mA, was selected as the X-ray source, to minimize interference caused by Co and Fe Auger lines [28]. Deconvolution of the Fe 2p region has been reported to be more difficult when an Al source is used [19]. With a slot aperture setting, the spectrometer was used in spectrum analyzer mode and hybrid lens mode. The charge neutralizer was set at a current of 2.1 A, a bias of 1.3 V, and a charge of 2.2 V during analysis. A survey scan (1 sweep/100 ms dwell) was acquired between 1200 and 0 eV. Concurrent sweeps for the La 3d (8/200), Sr 3d (8/150), Co 2p (8/800), Fe 2p (8/400), O 1s (8/75), and C 1s (8/150) regions were obtained. The C 1s peak at 284.5 eV was used for binding energy correction. The deconvolution was performed with Gaussian curves using the XPS Peak 4.1 program. Elemental surface composition was calculated using transmission values and relative sensitivity factors specific for the instrument and the Mg source.

### 2.4. Methanol oxidation activity

The catalytic activity of the samples was measured by methanol oxidation reactions. The reactions were performed with an Autochem II 2920 and a Cirrus residual gas-analyzing mass spectrometer (RGA-MS). Samples were loaded on an equal surface site basis ($2.0 \times 10^{17}$ sites) into U-tube reactors with the samples sitting on top of quartz wool. Samples were exposed to 10% $O_2$/He at 850 °C for 20 min before the reaction. After the pretreatment, the sample was exposed to the reaction mixture, which consisted of 10% $O_2$/He at 23 mL/min and He at 27 mL/min bubbled through the vapor generator. The generator was held at a constant temperature of 33 °C to provide excess methanol compared with oxygen. Using Antoine's equation, the methanol-to-oxygen ratio was found to be near 2. All lines beyond the generator were held at 110 °C. The reaction was performed using a quasi-steady-state approach. The reaction temperature was ramped linearly at 5 °C/min in 50 or 100 °C intervals, then held constant for 30 min. The RGA-MS was used to monitor the reactor effluent. The instrument was used in scanning ion mode with the electron multiplier detector. The signals were corrected using the ionization probability and fragmentation patterns for all ions present. The conversions, yields, and selectivities were calculated using the following expressions:

$$\%\ CH_3OH\ \text{conversion} = \frac{\text{mol of } CH_3OH \text{ converted}}{\text{mol of } CH_3OH \text{ fed}} \times 100,$$

$$\%\ O_2\ \text{conversion} = \frac{\text{mol of } O_2 \text{ converted}}{\text{total mol of } O_2 \text{ fed}} \times 100,$$

$$\%\ H_2\ \text{yield} = \frac{\text{mol of } H_2 \text{ produced}}{2 \times (\text{mol of } CH_3OH \text{ fed})} \times 100,$$

$$\%\ H_2\ \text{selectivity} = \frac{2 \times (\text{mol of } H_2 \text{ produced})}{\text{mol of H in all products}} \times 100,$$

$$\%\ CO_2\ \text{yield} = \frac{\text{mol of } CO_2 \text{ produced}}{\text{mol of } CH_3OH \text{ fed}} \times 100,$$

$$\%\ CO_2\ \text{selectivity} = \frac{\text{mol of } CO_2 \text{ produced}}{\text{mol of C in all products}} \times 100.$$

## 3. Results

### 3.1. Use of methanol as a probe molecule

An example of the chemisorption process is shown in Fig. 1a for $La_{0.6}Sr_{0.4}Co_{0.3}Fe_{0.7}O_{3-\delta}$. As demonstrated by methanol ($m/z = 32$ ($CH_3OH$)) and its fragments ($m/z = 15$ ($CH_3$), 29 (COH), and 31 ($CH_3O$)), slightly less than 2 complete pulses were adsorbed. Moreover, no peaks were detected for $CO_2$ ($m/z = 44$) besides a small amount of noise associated with the valve switch. Adsorption profiles for the main methanol fragment ($m/z = 31$ ($CH_3O$)) are shown in Fig. 1b for the different formulations. $La_{0.6}Sr_{0.4}Co_{0.1}Fe_{0.9}O_{3-\delta}$ demonstrated a greater adsorption capacity than the samples with larger amounts of Co. The adsorption amount was converted into surface site density as shown in the last column of Table 1 using the mass-specific surface areas. Generally, these values are low compared with traditional metal oxides [15]. The surface density measurements were reproduced for different batches of $La_{0.6}Sr_{0.4}Co_{0.2}Fe_{0.8}O_{3-\delta}$, and the values were found to be within 0.1 site/nm$^2$ of the results reported in Table 1.

After the surface was saturated with methanol as indicated by constant pulse areas, desorption profiles were obtained by TPD. Typical results are shown in Fig. 2 for $La_{0.6}Sr_{0.4}Co_{0.2}Fe_{0.8}O_{3-\delta}$. At low temperatures (80–150 °C), molecularly adsorbed methanol desorbed from the sample. These species have been commonly misidentified as physically adsorbed methanol, whereas they are actually intact Lewis-bound methanol adducts [16,17,29,30]. We present more detail on this topic when discussing the DRIFTS results. At intermediate temperatures (150–300 °C), chemisorbed methanol desorbed as $CO_2$ ($m/z = 44$) and $H_2O$ ($m/z = 18$). These products formed after a surface reaction of the chemisorbed methanol with available oxygen from the sample's lattice. No peaks were detected for formaldehyde ($m/z = 30$), a product of redox sites. Moreover, there was no evidence of acidic sites linked to dimethyl ether ($m/z = 46$). The peaks for $m/z = 45$ and 46 were accounted for by natural isotope levels of $^{13}C$ (~1%) and $^{18}O$ (~0.2%). Although high-temperature peaks (>300 °C) were seen for $m/z = 32$, these were not due to intact methanol de-

Table 1
Adsorption data (sites/nm$^2$) from adsorbed methanol on $La_{0.6}Sr_{0.4}Co_yFe_{1-y}O_{3-\delta}$

| $y$ | Lewis-bound | Basic | Total |
|---|---|---|---|
| 0.1 | 0.64 | 1.49 | 2.13 |
| 0.2 | 0.66 | 0.37 | 1.03 |
| 0.3 | 0.66 | 0.53 | 1.19 |

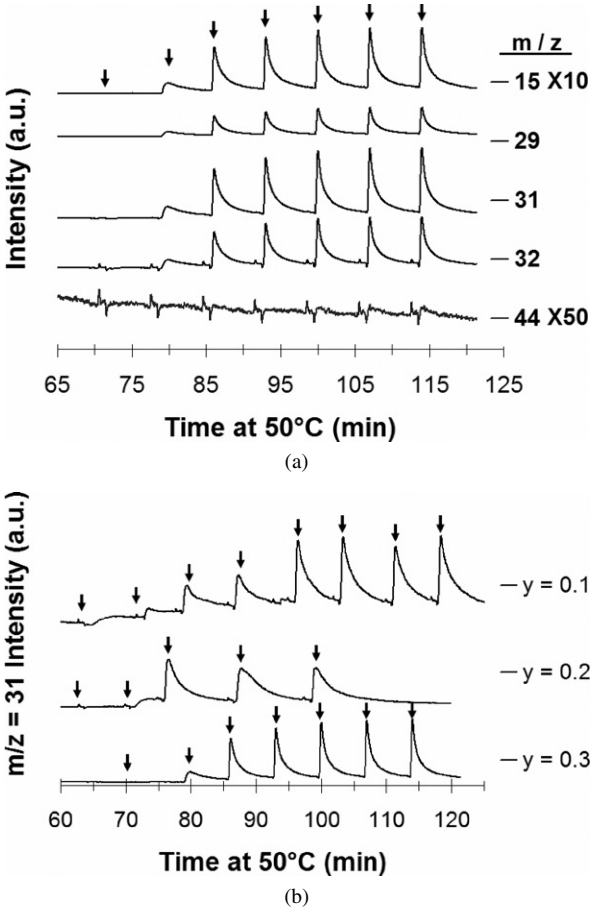


Fig. 1. Pulsed methanol chemisorption at 50 °C for $La_{0.6}Sr_{0.4}Co_yFe_{1-y}O_{3-\delta}$. (a) Monitoring of several ions for $y = 0.3$. (b) $m/z = 31$ for different formulations. Pulses indicated by arrows. Profiles are offset for clarity.

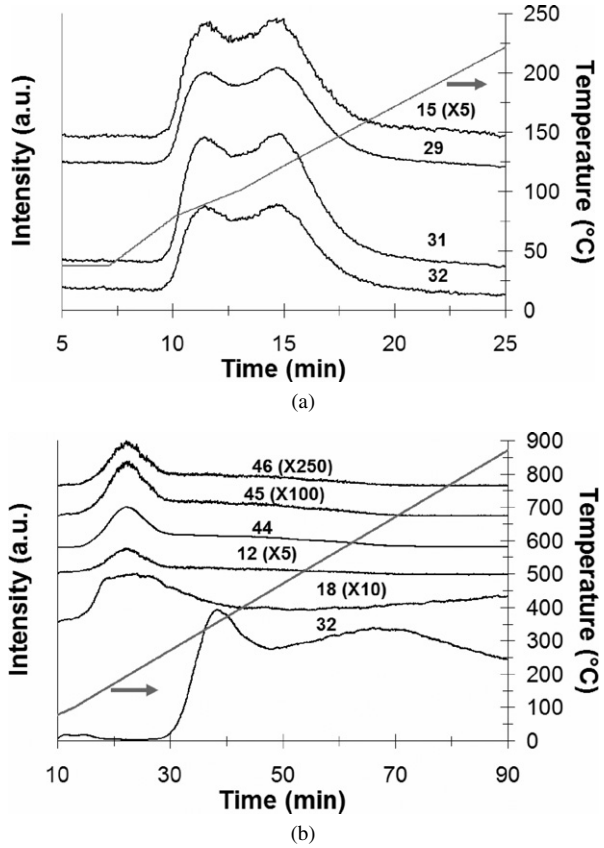


Fig. 2. Desorption of chemisorbed methanol from $La_{0.6}Sr_{0.4}Co_{0.2}Fe_{0.8}O_{3-\delta}$ as (a) intact methanol and (b) carbon dioxide and water after a surface reaction. Profiles are offset for clarity.

sorption. At these temperatures, lattice oxygen evolved from the bulk of the material to create oxygen vacancies [25]. Comparing the $m/z = 32$ profile obtained when no methanol was adsorbed in our previous work with the present profile shows that the relative amounts of oxygen desorbed at low ($\alpha$-oxygen) to high ($\beta$-oxygen) temperatures were different. Here $\alpha$-oxygen refers to the oxygen related to adsorbed or near-surface oxygen. High-temperature oxygen desorption or $\beta$-oxygen is associated with the transition metals on the B-site. Although more $\beta$-oxygen desorbed when no methanol was present, $\alpha$-oxygen became the primary desorbing species after methanol desorption. The results suggested that the lattice oxygen replenished the near-surface oxygen that was consumed to oxidize $CH_3OH$ to $CO_2$ and $H_2O$, and that oxygen vacancies were more likely to form in the bulk than at or near the surface after oxidation of the methoxy surface species.

Fig. 3 compares the desorption profiles as a function of Co content. As we discuss in the DRIFTS results section, this species that desorbed at lower temperatures was a Lewis-bound species. With the Lewis-bound sites quantified, it was possible to back-calculate the basic site density. The nature of the sites is broken down in Table 1. Whereas the peak temperature remained constant for the three samples, the intensity of the $CO_2$ desorption profiles followed the same trend as the basic site density. All three samples demonstrated smaller desorption peaks at higher temperatures than the major peak. These additional peaks show that some sites have stronger interactions and indicate at least some surface heterogeneity.

As alluded to earlier, DRIFTS studies confirmed the nature of surface species. DRIFT spectra for the desorption of methanol are shown in Fig. 4. In the high wavenumber region, $CH_3$ (~2900 $cm^{-1}$) and OH (~3700 $cm^{-1}$) vibrations indicated the presence of adsorbed methanol at low temperatures. Similarly, adsorbed methanol species was signified by the CO vibrations (~1050 $cm^{-1}$) in the low wavenumber region. As the temperature was raised, the bands corresponding to surface species decreased and the $CH_3$ and OH vibrations were no longer present by 150 °C. Moreover, $CO_2$ (~2350 $cm^{-1}$) appeared in the spectrum obtained at 125 °C and existed during the rest of the experiment. The wide temperature range of $CO_2$ reinforced the idea of surface heterogeneity. For solid solutions of perovskite-type materials, a heterogeneous surface was easily realized through Sr-doping, which created a mix of trivalent and tetravalent B-site cations. Because the methanol desorbed molecularly as methanol and as $CO_2$ after surface reaction of a methoxy species with oxygen from the sample, it was not surprising that the $CH_3$ vibrations were nearly extinct before the $CO_2$ evolved. A more in-depth examination of the $CH_3$ vibra-

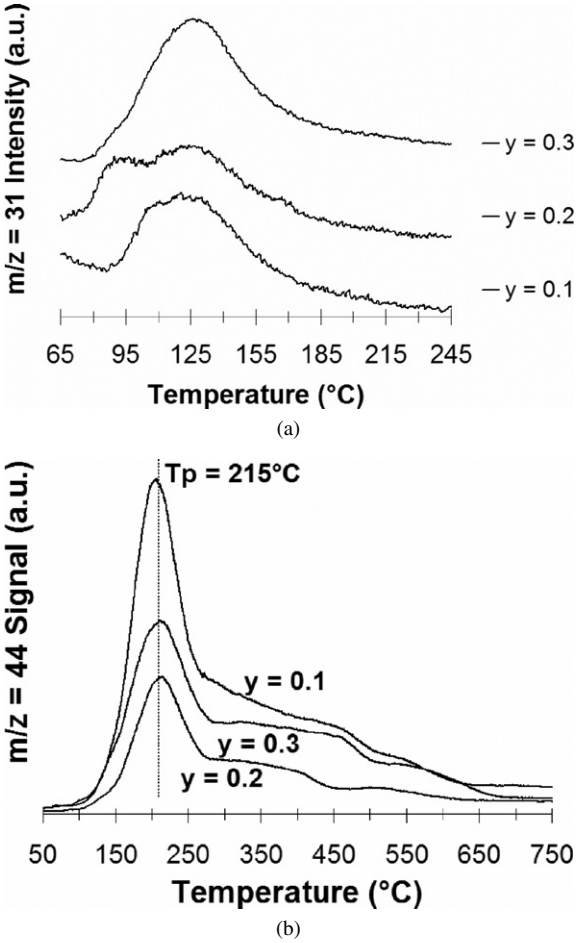


Fig. 3. Desorption of chemisorbed methanol for $La_{0.6}Sr_{0.4}Co_yFe_{1-y}O_{3-\delta}$. (a) Intact methanol desorption. (b) $CO_2$ formation after surface reaction.

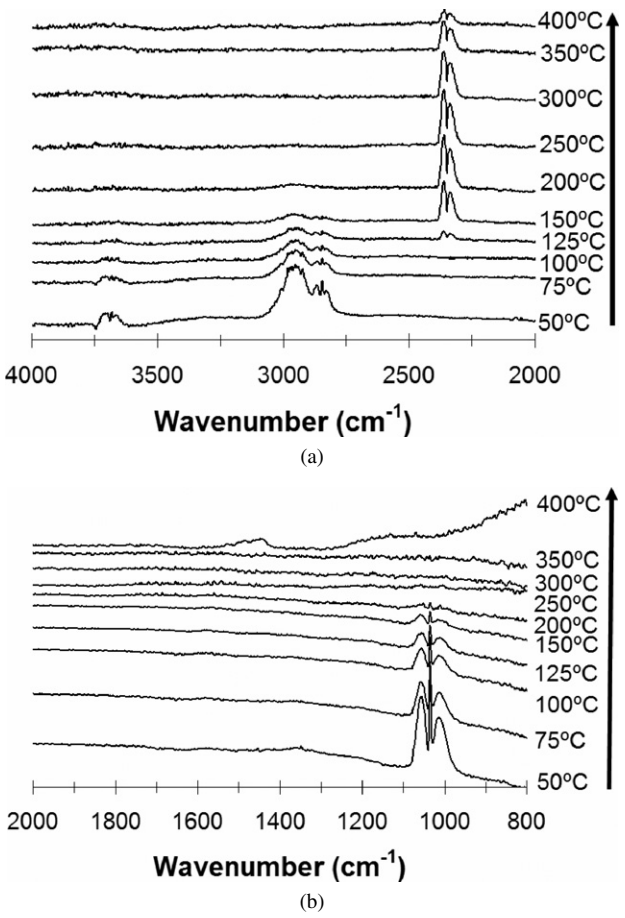


Fig. 4. Methanol TPD from $La_{0.6}Sr_{0.4}Co_{0.2}Fe_{0.8}O_{3-\delta}$ in DRIFTS. (a) High wavenumber region and (b) low wavenumber region. Profiles are offset for clarity.

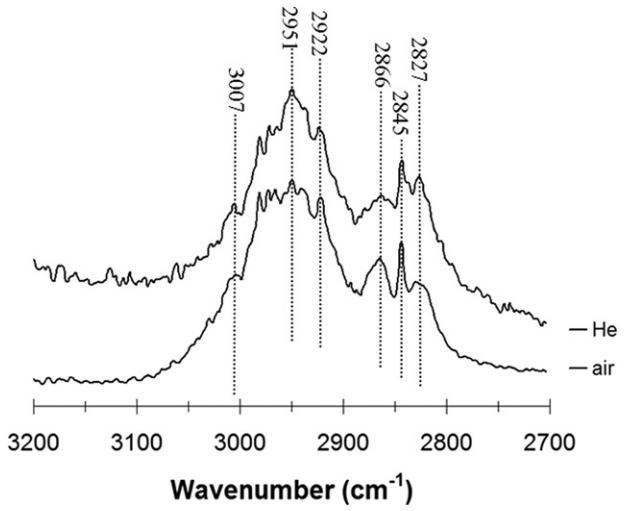


Fig. 5. $CH_3$ vibrations for adsorbed methanol species at 50 °C following different treatments at 550 °C on $La_{0.6}Sr_{0.4}Co_{0.2}Fe_{0.8}O_{3-\delta}$ in DRIFTS. Spectra are offset for clarity.

Table 2
DRIFTS band assignments for Fig. 5

| Band ($cm^{-1}$) | Vibration |
|---|---|
| 3007 | Asymmetric $CH_3$ stretch |
| 2951 | Symmetric $CH_3$ (LB) stretch |
| 2922 | Symmetric $CH_3$ stretch |
| 2866 | Asymmetric $CH_3$ bend |
| 2845 | Symmetric $CH_3$ (LB) bend |
| 2827 | Symmetric $CH_3$ bend |

tions yielded important information on the types of adsorbed methanol species.

The $CH_3$ vibrations are shown in much greater clarity in Fig. 5. Results are shown after the adsorption of methanol when an oxidative (air) and an inert (He) environment (at 550 °C in both cases) were used before adsorption. Band assignments for the $CH_3$ region are presented in Table 2. The band designations have been compiled from literature on methanol–oxide surface interactions [29,30]. The presence of both surface methoxy and molecularly adsorbed or Lewis-bound (LB) species has been identified. The Lewis-bound methanol species are signified by the relatively sharp bands at 2951 and 2845 $cm^{-1}$. Generally, the undissociated Lewis-bound methanol species are found at slightly lower frequencies than the surface methoxy species [16]. Moreover, undissociated adsorbed methanol species have a sharp CO vibration near 1030 $cm^{-1}$ [16]. Fig. 4 shows that the sharp CO vibration existed at 1037 $cm^{-1}$. The bands at 2827, 2866, 2922, and 3007 $cm^{-1}$ were associated with various stretches and bends (first overtones) of surface methoxy species. With these designations, likely surface structures for the different types of adsorbed methanol are formulated in Scheme 1. Reviews by Lavalley and Busca were instrumental in constructing the surface structures [16,17].

Besides methanol adsorbing as two different types of surface species, the methoxy species led to $CO_2$ evolution over a wide range of temperatures. Similar types of desorption behavior has been reported for perovskite-type materials when $CO_2$

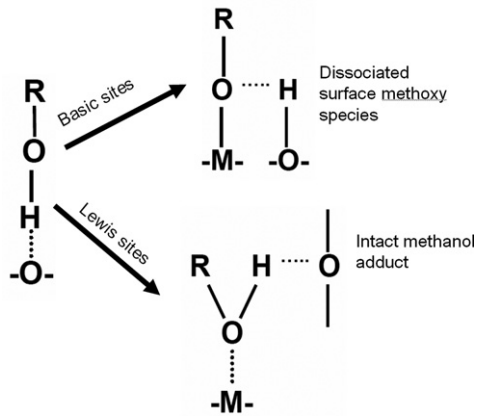


Scheme 1. Types of surface species formed during methanol adsorption.

was used as the probe molecule [2]. In this review by Pena and Fierro, desorption below 152 °C was linked to monodentate carbonates, and desorption at 267–647 °C was speculated to occur due to decomposition of a combination of bidentate and bridged carbonates. Generally, these desorption peaks fit with the temperature ranges given in Fig. 3b. Moreover, the bidentate and bridge carbonates were linked to the extent of the oxide reduction in the samples [2]. For this reason, the study was reexamined after exposure to an inert environment at elevated temperatures (550 °C), as shown in Fig. 5, to look for effects caused by oxygen vacancies. $La_{0.6}Sr_{0.4}Co_{0.2}Fe_{0.8}O_{3-\delta}$ has been shown to be nearly stoichiometric with respect to oxygen content at this temperature in air, whereas a significant amount of oxygen vacancies form in He [25]. Whereas the bulk and surface defects may not be exclusively linked (e.g., surface vacancies may exist even when the bulk is fully oxidized or vice versa), the amount of surface vacancies should increase as oxygen vacancies form in the bulk.

Based on the two surface structures, one would intuitively expect a more oxidized surface to lead to the dissociated surface methoxy species, because oxygen is available to extract hydrogen from methanol. For similar reasoning, formation of the Lewis-bound methanol species would be favored on a less-oxidized surface. Looking at the bands for $CH_3$ stretching, the intensities of the bands for Lewis-bound species remained relatively constant compared with the bands for the methoxy species as the environment before methanol adsorption was changed. The lack of differences is explained by the replenishment of the surface and near-surface oxygen with the lattice oxygen, which was in agreement with the TPD data and SrO suboxide present at the surface (discussed in Section 3.2). Because no bands for carbonate species were detected (due to dark samples with low surface areas), direct assertions cannot be reached for the intermediates between the methoxy species and $CO_2$. Instead, it can only be inferred from the TPD that the major species involve a monodentate carbonate, whereas smaller amounts of more stable bidentate or bridged carbonates exist.

### 3.2. Surface characterization using XPS

Examples of the peak deconvolution and spectra compared as a function of Co content are shown in Figs. 6–8, with the

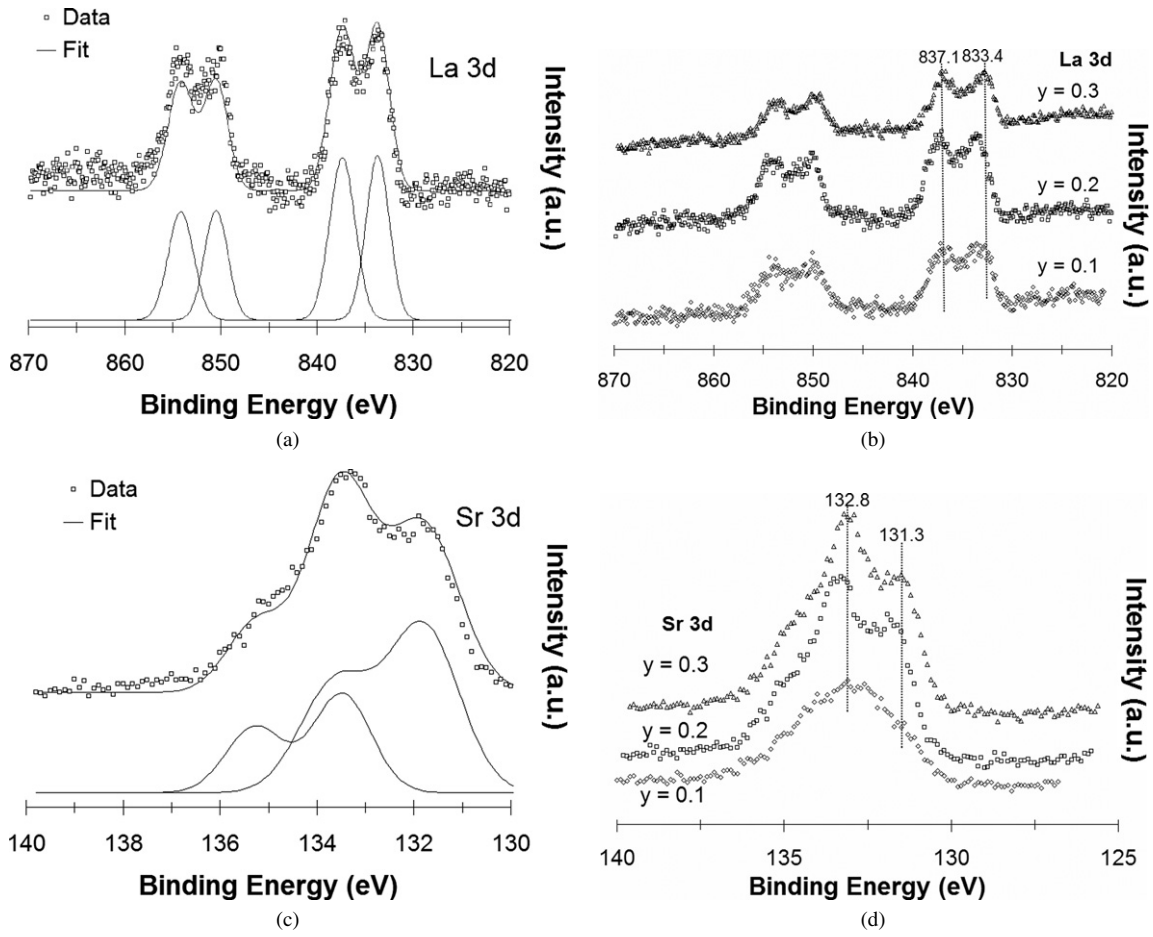


Fig. 6. X-ray photoelectron spectra for A-site constituents of $La_{0.6}Sr_{0.4}Co_yFe_{1-y}O_{3-\delta}$. (a) Deconvolution for La 3d when $y = 0.2$. (b) Comparison of La 3d region for different B-site compositions. (c) Deconvolution for Sr 3d when $y = 0.2$. (d) Comparison of Sr 3d region for different B-site compositions. Spectra are offset for clarity.

Table 3
XPS peak parameters extracted from Figs. 6–8

| Region | Position (eV) | | | Surface composition (%) | | |
|---|---|---|---|---|---|---|
| | $y = 0.1$ | $y = 0.2$ | $y = 0.3$ | $y = 0.1$ | $y = 0.2$ | $y = 0.3$ |
| La $3d_{5/2}$ | 833.1 | 834.3 | 833.2 | 3.6 | 1.2 | 2.0 |
| | 836.7 | 837.7 | 837.0 | 3.8 | 5.2 | 2.3 |
| Total | | | | 7.3 | 6.4 | 4.3 |
| Sr $3d_{5/2}$ | 132.5 | 131.8 | 131.6 | 13.4 | 7.8 | 8.5 |
| | | 133.4 | 133.1 | | 5.7 | 7.4 |
| Total | | | | 13.4 | 13.5 | 15.9 |
| Co $2p_{3/2}$ | 780.1 | 780.2 | 780.1 | 0.5 | 1.3 | 1.1 |
| Fe $2p_{3/2}$ | 710.0 | 709.9 | 709.7 | 6.4 | 5.8 | 5.3 |
| O 1s | 529.4 | 530.5 | 528.2 | 43.0 | 29.7 | 24.3 |
| | 531.9 | 533.2 | 531.0 | 29.3 | 43.4 | 49.1 |
| Total | | | | 72.3 | 73.1 | 73.4 |

A-site cations in Fig. 6, the B-site cations in Fig. 7, and oxygen in Fig. 8. The spectra for each sample were deconvoluted as shown in the example. The peak positions and the elemental surface compositions extracted from the spectra deconvolution are given in Table 3.

La existed in two forms: a trivalent oxide with a $3d_{5/2}$ binding energy near 833.5 eV and a less-oxidized form near 837 eV that could be caused by hydroxyl formation [28,31]. Whereas the positions did not change with Co content, the surface composition did. Sr existed in two divalent oxide forms with $3d_{5/2}$ binding energies at 131.5 and 133.2 eV. These values match those reported for $La_{0.4}Sr_{0.6}Co_{0.8}Fe_{0.2}O_{3-\delta}$, and the two peaks may arise from Sr in the perovskite phase and a suboxide phase (although the presence of surface carbonates cannot be excluded) [31]. The Sr-based suboxide phase, which may be less likely to form oxygen vacancies than the perovskite-type phase, may explain why the surface appeared less likely to form oxygen vacancies than the bulk. The Co $2p_{3/2}$ peaks were slightly above 780 eV. Values near ~779.5 eV have been reported for trivalent species in $Co_2O_3$ and $LaCoO_3$ [1,28]. A small shift [31] toward higher binding energy may indicate the presence of tetravalent species that formed through Sr doping. A value of 780.2 eV was reported for $La_{0.4}Sr_{0.6}Co_{0.8}Fe_{0.2}O_{3-\delta}$ [31]. As demonstrated by the lack of the satellite peaks near 787.5 eV, divalent Co, an indicator of impurities at the surface, was not present [1,19]. The Fe $2p_{3/2}$ peaks were near 710 eV. Although none of the usual Fe species are in this region, the location fits well with the values given for perovskite-type oxides with only La on the A site [19,28,31]. The O 1s region exhibited the most interesting surface behavior, with large shifts detected as a function of Co content. The low

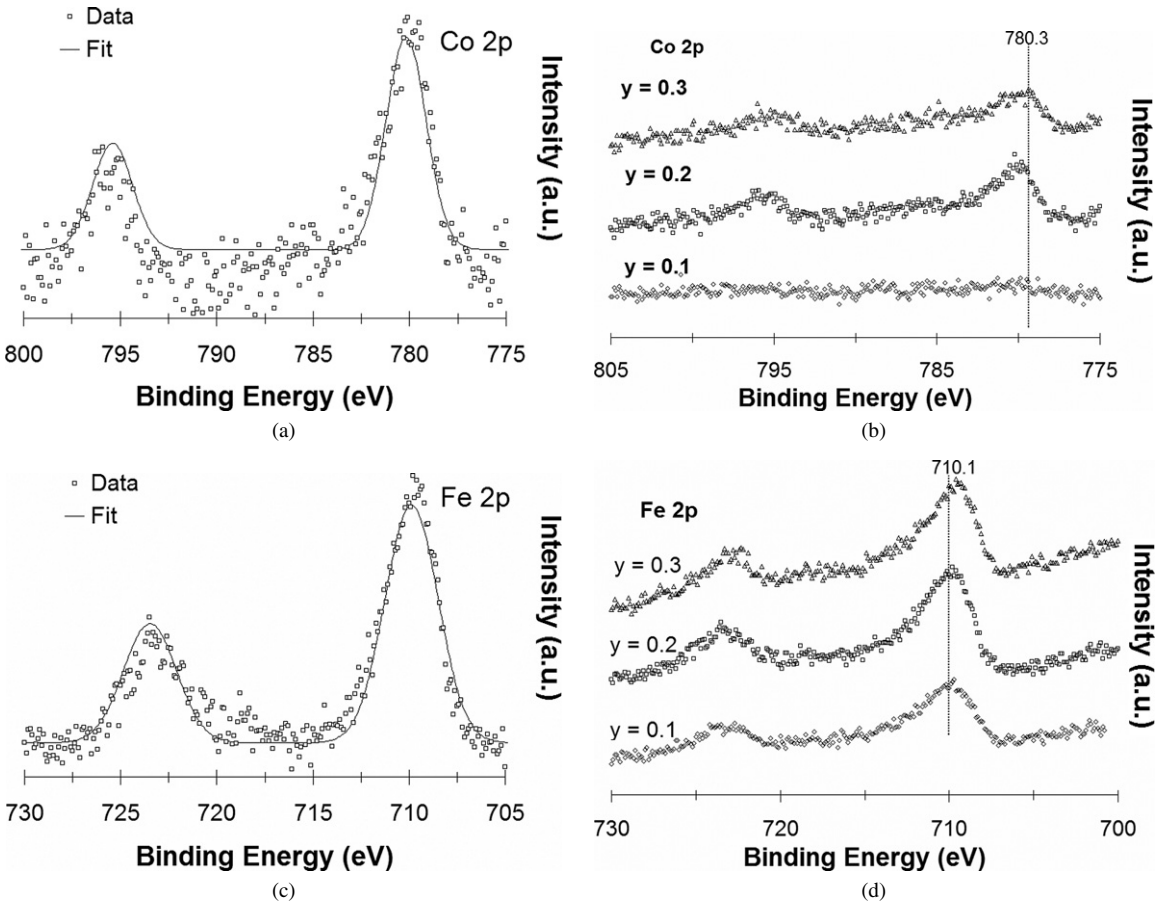


Fig. 7. X-ray photoelectron spectra for B-site constituents of $La_{0.6}Sr_{0.4}Co_yFe_{1-y}O_{3-\delta}$. (a) Deconvolution for Co 2p when $y = 0.2$. (b) Comparison of Co 2p region for different B-site compositions. (c) Deconvolution for Fe 2p when $y = 0.2$. (d) Comparison of Fe 2p region for different B-site compositions. Spectra are offset for clarity.

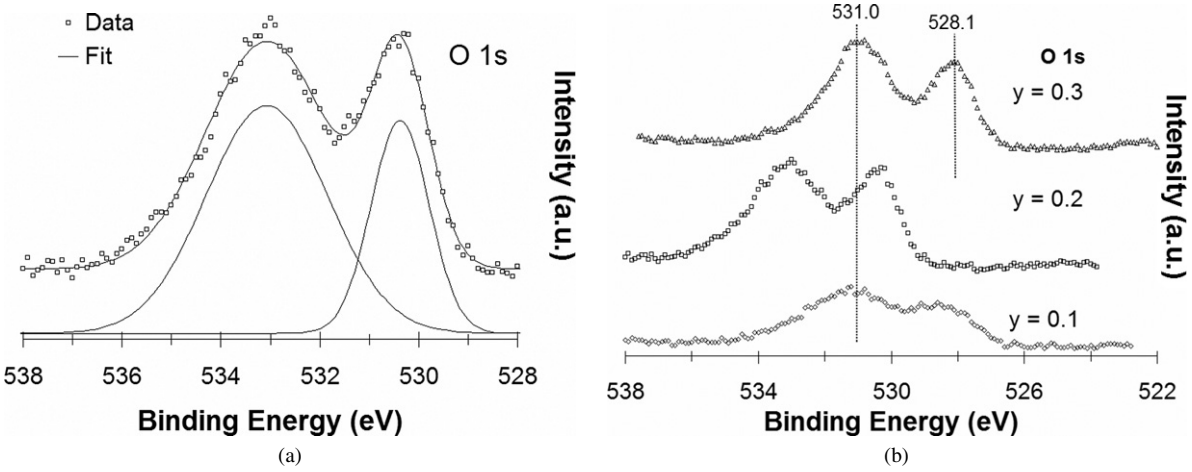


Fig. 8. O 1s region in X-ray photoelectron spectra for $La_{0.6}Sr_{0.4}Co_yFe_{1-y}O_{3-\delta}$. (a) Deconvolution for O 1s when $y = 0.2$. (b) Comparison of O 1s region for different B-site compositions. Spectra are offset for clarity.

binding energy peak correlated to anion network of lattice oxide ions in the perovskite structure [31,32]. The shifts displayed the same trend as the bulk reducibility determined by TPR [25]. The high binding energy peak is related to chemisorbed oxygen species.

The surface composition of perovskite-type materials have been known to deviate from the bulk composition [3], and our present findings are in agreement with these conclusions. The results given in Table 3 demonstrate relatively good agreement with the composition expected from the perovskite phase (i.e., 20% A site, 20% B site, and 60% anions), but also demonstrate deviations from the bulk as O became enriched at the surface in comparison to the transition metals. Excess oxygen at the surface may be correlated with the fact that the surface is less

Partial methanol oxidation:
$CH_3OH + \frac{1}{2}O_2 \rightarrow CO_2 + 2H_2$,
$CH_3OH + O_2 \rightarrow CO_2 + H_2 + H_2O$,
$CH_3OH + \frac{1}{2}O_2 \rightarrow CO + H_2 + H_2O$.

Complete methanol oxidation:
$CH_3OH + \frac{3}{2}O_2 \rightarrow CO_2 + 2H_2O$.

Methanol decomposition:
$CH_3OH \rightarrow CO + 2H_2$.

CO oxidation:
$2CO + O_2 \rightarrow 2CO_2$.

$H_2$ oxidation:
$2H_2 + O_2 \rightarrow 2H_2O$.

Water–gas shift:
$CO + H_2O \rightarrow CO_2 + H_2$.

Methanol steam reforming:
$CH_3OH + H_2O \rightarrow CO_2 + 3H_2$.

Scheme 2. Possible reactions for methanol oxidation.

likely to contain anion vacancies (from differences in O-TPD with and without methanol adsorption). Moreover, Sr was enriched at the surface relative to La, and a surface enriched in the dopant may be responsible for the differences in oxygen vacancy preference between the surface and the bulk.

### 3.3. Catalytic activity

Methanol oxidation was selected as a model reaction (important reactions shown in Scheme 2) to link the reaction performance to measured properties. All three samples showed the same general trends as discussed here unless noted otherwise. Appreciable reactant conversions were first observed at 250 °C. At low methanol conversions (and, consequently, low temperatures), the complete oxidation reaction occurred, as demonstrated by high $CO_2$ and low $H_2$ selectivities. $H_2$ and CO were not detected until 350 °C. The results at 300–400 °C are discussed in more detail later, because the primary differences between samples were observed in this temperature range. The methanol conversion was further increased by raising the temperature, and the primary products changed. At 500 °C, the $CO_2$ yield progressed through a maximum. Also at this temperature, $H_2$ became the predominant product. At all temperatures, oxygen was converted at higher rates than methanol. At 500 °C, the maximum in the $CO_2$ yield aligned with the oxygen conversion, reaching nearly 100%. Only ∼75% of the methanol was converted. Thus, the oxidized products were favored when the methanol conversion lagged behind the oxygen conversion. Moreover, any oxygen escaping from the lattice in conjunction with the formation of oxygen vacancies also would shift the reaction toward the oxidized productions. At 600 and 700 °C, $H_2$ was even more favored over $H_2O$, whereas CO and $CO_2$ formed almost evenly. There was no longer a preference for the formation of oxidized products, because the methanol and oxygen conversions were 100%. Because the product distribution from the partial oxidation can be different (as demonstrated in Scheme 2), it is noteworthy that the catalysts showed a slight preference for forming $CO_2$ compared with $H_2O$ at complete conversion.

Because single carbon (C1) chemistry can be significantly more complex [33] than discussed in Scheme 2, we briefly discuss the apparently nonoperative reactions. Although the studies were performed on Co- or Fe-based materials, other perovskite-type oxides also have been used for converting methanol to methyl formate and formaldehyde, with the possibility of dimethyl ether and methane impurity formation [34–37]. Methane formed through the dry reforming of methyl formate [34]. Perovskite-type oxides also exhibited activity for hydrogenation, hydrogenolysis, and oxidative coupling reactions [2,33]. Consistent with the TPD studies, neither dimethyl ether nor formaldehyde formed under the conditions used in this study. On the other hand, small amounts of methyl formate and methane formed at 450 and 500 °C, respectively. Thus, it is possible that similar behavior occurred as has been reported for Cu perovskite-type oxides [34]. Because basic metal oxides have been linked to the direct dehydrogenation of methanol to make methyl formate [34], its formation was not unexpected. However, the presence of these species was small, and the samples behaved primarily as total oxidation catalysts.

In the absence of a complete reaction network analysis, several test reactions were monitored through temperature-programmed reactions (100 mg, 10 °C/min from 50 to 700 °C, and each reactant at 5% with He balance) for $La_{0.6}Sr_{0.4}Co_{0.2}Fe_{0.8}O_{3-\delta}$. This sample exhibited good activity for CO oxidation and the water–gas shift reaction, but poor activity for methane-steam reforming. Activity for CO oxidation and the water–gas shift reactions began at 215 and 450 °C and maximum conversion was obtained at 450 and 550 °C, respectively. The sample exhibited no activity for methane-steam reforming below 700 °C. It is also worth noting that exposure to 50 ppm $H_2S/N_2$ at 700 °C for 5 h had a minimal impact on the results; for example, it shifted the CO oxidation profiles toward higher temperatures by only roughly 50 °C and had no effect on the water–gas shift results. Moreover, the samples demonstrated no signs of coking when TPO experiments were conducted after steady reaction at 700 °C for 4 h.

The reaction results for methanol oxidation are shown in Table 4 as a function of temperature (300, 350, and 400 °C) and Co content. At these temperatures, the intermediate Co content led to the highest methanol and oxygen conversions. In addition, the high-Co loading sample had better activity than the low-Co loading sample. Thus, these results were consistent with property changes that do not scale proportionally to the Co content.

## 4. Discussion

We discuss the differences in the surface properties, with an emphasis on trends with surface basicity and oxygen storage capacity and influence of a potential electronic structure transition that occurred with Co content. We compare the catalytic properties for the oxidation of volatile organic compounds with

Table 4
Reaction comparison[a] for methanol oxidation

| Catalyst $La_{0.6}Sr_{0.4}Co_yFe_{1-y}O_{3-\delta}$ | Conversion (%) | | Yield (%) | | Selectivity (%) | |
|---|---|---|---|---|---|---|
| | $CH_3OH$ | $O_2$ | $H_2$ | $CO_2$ | $H_2$ | $CO_2$ |
| | $T = 300\,^\circ C$ | | | | | |
| $y = 0.1$ | 6 | 15 | 0 | 7 | 6 | 100 |
| $y = 0.2$ | 23 | 36 | 0 | 12 | 0 | 100 |
| $y = 0.3$ | 7 | 16 | 0 | 5 | 0 | 100 |
| | $T = 350\,^\circ C$ | | | | | |
| $y = 0.1$ | 12 | 31 | 1 | 17 | 10 | 100 |
| $y = 0.2$ | 44 | 80 | 6 | 39 | 30 | 95 |
| $y = 0.3$ | 28 | 56 | 2 | 29 | 11 | 97 |
| | $T = 400\,^\circ C$ | | | | | |
| $y = 0.1$ | 34 | 68 | 6 | 37 | 25 | 92 |
| $y = 0.2$ | 46 | 86 | 10 | 45 | 39 | 92 |
| $y = 0.3$ | 44 | 83 | 10 | 47 | 34 | 91 |

[a] Reaction conditions: $CH_3OH/O_2/He = 10.5/4.9/84.6$, feed flow rate = 50 mL/min, and equal surface sites.

Table 5
Surface area-normalized reaction rates and turnover frequencies for methanol oxidation

| Catalyst $La_{0.6}Sr_{0.4}Co_yFe_{1-y}O_{3-\delta}$ | Methanol rate (mL methanol/($m^2$ min)) | Methanol TOF ($s^{-1}$) |
|---|---|---|
| | $T = 300\,^\circ C$ | |
| $y = 0.1$ | 0.4 | 0.07 |
| $y = 0.2$ | 6.6 | 2.56 |
| $y = 0.3$ | 2.4 | 0.81 |
| | $T = 350\,^\circ C$ | |
| $y = 0.1$ | 0.7 | 0.14 |
| $y = 0.2$ | 12.7 | 4.90 |
| $y = 0.3$ | 9.6 | 3.23 |
| | $T = 400\,^\circ C$ | |
| $y = 0.1$ | 2.1 | 0.39 |
| $y = 0.2$ | 13.3 | 5.13 |
| $y = 0.3$ | 15.2 | 5.07 |

other perovskite-type oxides used in similar reactions. We also address differences in preparation techniques.

### 4.1. Catalytic applications of doped $LaFeO_3$ materials

We compared the Sr- and Co-doped samples with available results for similar reactions as reported in the literature over perovskite-type oxides and found that the samples studied in this work were generally less active. Compared with $LaNiO_3$, methanol conversions lagged behind by roughly 100 °C, but the differences more than likely can be attributed to the low flow rate (4 mL/min) used in the study (insufficient information given to compare the surface area-normalized reaction rate or TOF) [36]. Higher temperatures were needed to achieve similar methanol oxidation activity compared with $La_{0.6}Sr_{0.4}MnO_3$, which gave 50% methanol conversion at 164 °C, the temperature at which methanol conversion became significant in the present study and a similar result as that for precious metal catalysts supported on $Al_2O_3$ [38]. $La_{0.6}Sr_{0.4}Co_{0.2}Fe_{0.8}O_{3-\delta}$ was also less active than $LaMnO_3$ for CO oxidation, because 100% conversion was achieved near 150 °C [39] or about 100 °C before $La_{0.6}Sr_{0.4}Co_{0.2}Fe_{0.8}O_{3-\delta}$ achieved significant conversion levels. Surface area-normalized methanol oxidation rates have been reported for formulations of $LnTmO_3$ where Ln = La, Sm, and Gd and Tm = Co, Mn, and Fe [18] at 200 °C and the rates determined for $La_{0.6}Sr_{0.4}Co_{0.2}Fe_{0.8}O_{3-\delta}$ in the present study, possibly caused by Sr doping, are two orders of magnitude greater. At this temperature, 4% of the methanol was converted, which led to a rate of 1.1 mL methanol/($m^2$ min). For future comparisons, the reaction results have been converted in Table 5 into surface area-normalized reaction rates and turnover frequencies using the total surface site density.

Several possible reasons are proposed to explain why the Co- and Fe-based materials in this study have lower catalytic activity than those referenced earlier in this section. First, Fe-based perovskite-type oxides have been shown to have lower oxidation activity than Co- or Mn-based materials [2]. This trade-off is necessary to balance catalytic activity with anionic conduction and thermal stability. Second, the samples were prepared through a solid-state route, as opposed to alternative methods that can yield higher surface areas. In addition to its simple nature, this preparation method was used, because low surface area applications are of primary interest, deactivation through sintering is minimized, and the lower cost of precursors makes this route more economically feasible for commercialization. Nonetheless, the preparation of perovskite-type oxides with high surface areas while also maintaining good stability is important and currently under study [3,19,40].

Despite the worse performance compared with previously reported studies, the samples still may have catalytic applications due to their high thermal stability. As discussed previously [25], $La_{0.6}Sr_{0.4}Co_{0.2}Fe_{0.8}O_{3-\delta}$ was stable under reducing conditions up to 800 °C. Such stability is much higher than that for many perovskite-type oxides and allows the use of these samples in applications in which reducing conditions prevail and the sample's robust nature is exploited. For example, these materials could be used as part of bifunctional catalysts for autothermal reforming, where hydrogen is produced and high local temperatures may exist due to the exothermic nature of the oxidation reaction. Moreover, the high oxygen mobility may allow for low carbon deposition rates for both catalysts, provided that good mixing allows for oxygen spillover from the perovskite-type oxide. These materials also have been considered as SOFC anode materials [41,42]. In these studies, the materials were found to have similar $CH_4$ and CO oxidation activity compared with the conventional SOFC anode material, Ni-YSZ.

### 4.2. Trends with oxygen storage capacity and surface basicity

For the three samples of the form $La_{0.6}Sr_{0.4}Co_yFe_{1-y}O_{3-\delta}$ studied in this work, the methanol and oxygen reactivity in the temperature range of 300–400 °C decreased in the following order: $y = 0.2 > y = 0.3 > y = 0.1$. Because this trend is nonlinear with respect to Co content, it is desirable to correlate the interesting behavior with bulk and surface properties. Oxidation activity for methane [43,44] and propane [22] has been linked

to oxygen storage capacity. However, the surface composition and basicity also may be influential in controlling activity.

As shown in our earlier study [25], the anion lattice is able to store several different types of oxygen. The oxygen desorbed at lower temperatures or $\alpha$-oxygen is the oxygen that is related to adsorbed or near-surface oxygen. The amount of $\alpha$-oxygen was inversely related to the methanol oxidation activity and decreased in the following order: $y = 0.3 > y = 0.1 > y = 0.2$. High-temperature oxygen desorption or $\beta$-oxygen is associated with the transition metals on the B site. The amount of $\beta$-oxygen desorption was found to be in agreement with the trend in reaction activity, thus confirming the association between oxygen storage capacity and oxidation activity. Such an explanation indicates an interfacial mechanism in which the high oxygen mobility supplies available oxygen to oxidize methanol rather than less mobile adsorbed oxygen species; that is, oxygen is reduced and placed into the lattice at a faster rate than it can directly react with surface methoxy species.

That the Lewis sites were relatively constant was not surprising, because the samples contained the same amount of Sr. The addition of Sr (+2) into the La (+3) matrix is known to cause charge imbalances (either oxidation of the B-site transition metal or oxygen vacancies) compared with a pure La material. These samples have been determined to maintain stoichiometry with respect to oxygen under ambient conditions despite the change in Co content [25].

Because methanol is a slightly acidic molecule, a certain degree of basic strength is needed from the oxide surface to activate methanol (i.e., proton extraction) and form a surface methoxy species. Because the materials have nearly the same total site density (i.e., the composition variations change the unit cell by only a small amount), the greater amount of basic site density implies that more sites are above the minimum basicity threshold for methanol activation. Thus, the basic site density can be used as a benchmark for basic strength of the surface and is inversely related to methanol and oxygen conversions. Because highly basic sites should be better at proton extraction from methanol, the fact that the results did not follow this trend points to a mechanism in which oxygen mobility is more important than methanol activation.

The trends in the density and nature of surface sites have been correlated to surface concentrations measured by XPS. The amount of basic sites was determined to be a strong function of Co content, indicating that B-site composition exerted a greater influence on the surface properties. Co at the surface mirrored the reaction activity and was inversely related to the surface basicity. Thus can be explained by the fact that Co is generally more difficult to oxidize than Fe. Thus, the increased surface Co may be linked to more surface oxygen vacancies under reaction conditions that allow for more rapid incorporation of oxygen into the lattice.

For ideal perovskite-type materials, the distance between B-site cations is approximately 4 Å regardless of composition and environment. Using this value, a site existed every 3–5 unit cells. Consequently, there is the possibility of further modifying the surface so that the active sites approach one per unit cell. Moreover, the relative surface diffusion mobility can be inferred from the site density. Surface diffusion rates are difficult to measure, and thus a gap exists in the literature on this topic. As the surface basicity increases, the surface oxygen species are perhaps more stable and less likely to move freely, whereas weakly basic sites allow for high surface diffusion rates.

### 4.3. Influence of electronic structure transition

As mentioned previously [25], an electronic structure transition is expected to occur in the range of Co levels studied in this work. Pure Fe perovskite-type materials are localized electron conductors, whereas pure Co material exhibit delocalized electronic conduction [12]. The delocalized electronic structure has been shown to dominate at Fe levels <60% of the B site [45], so the transition occurs between the formulations of $La_{0.6}Sr_{0.4}Co_{0.4}Fe_{0.6}O_{3-\delta}$ and $La_{0.6}Sr_{0.4}FeO_{3-\delta}$. It should be noted that the compositions used in this study fall within this range. The fact that the properties evaluated in the present work (e.g., methanol oxidation activity, reducibility, surface basicity, oxygen storage capacity) did not exhibit trends proportional to the compositional changes (i.e., a maximum was observed) suggests that changes in the electronic structure might play an important role.

Previous studies on Co- and Fe-based perovskite-type oxides have proposed Co charge disproportionation, ionic factors, and a preferential charge compensation of Fe over Co [46,47]. Moreover, the nonlinear behavior of Co-rich formulations ($LaCo_{1-y}Fe_yO_{3-\delta}$ where $y = 0.1$) has been explained by the electronic structure complexity caused by low Fe content [19]. Merino et al. explained that compensation occurred with the $Co^{3+}$ (high-spin state)–$Co^{III}$ (low-spin state) pair at low Fe content, whereas $Fe^{4+}$ compensation dominated at higher Fe content. The electronic structures of $(La,Sr)CoO_{3-\delta}$ and $(La,Sr)FeO_{3-\delta}$ have been thoroughly studied by experimental and theoretical means [48–58]. As reported by those studies, a transition from $Co^{III}$ (low-spin state) to $Co^{3+}$ (high-spin state) was thermally induced for pure La-based materials, and more complicated behavior was seen when Sr doping was involved. Moreover, these studies observed that charge disproportionation between $Fe^{3+}$ and $Fe^{5+}$ can occur under certain compositions and conditions. Because no studies have been performed at La:Sr = 3:2 and an A-site charge imbalance has been shown to be instrumental to an electronic structure change, pinpointing the exact cause of the observed behavior is difficult [46,47]. But because the nonlinear behavior occurred at both ends of the composition range ($LaCo_{0.9}Fe_{0.1}O_{3-\delta}$ [19] and $La_{0.6}Sr_{0.4}Co_{0.1}Fe_{0.9}O_{3-\delta}$ [25] and the present study), it is plausible that electronic structure complexity arose due to the unusual charge balance behavior caused by slight B-site compositional changes.

## 5. Conclusion

The surface properties of $La_{0.6}Sr_{0.4}Co_yFe_{1-y}O_{3-\delta}$ with $y =$ 0.1, 0.2, and 0.3 were examined using methanol as a probe molecule, by XPS, and by methanol oxidation activity. The findings demonstrate that methanol is an appropriate probe

molecule for measuring surface site type and density in mixed perovskite-type oxides, expanding the use of this approach from supported and bulk metal oxides to more complex oxide structures. The different nature of these sites is likely to have important implications, leading to different activities for different reactions.

The nonlinear trend in catalytic activity with respect to Co content was found to agree with several measured parameters, such as strength of basic surface sites, reducibility, oxygen storage capacity, and B-site composition at the surface. These trends were linked to a possible electronic structure transition, which is supported by data in the literature. These findings may have important implications in pinpointing this transition in the composition range and establishing linkages to the chemical properties. Although the activity measured in this study was lower than reported for other perovskite-type oxides for similar reactions, these materials may have catalytic applications where their robustness is used.

## Acknowledgments

Financial support was provided by the Ohio Coal Development Office and the Ohio Department of Development through the Wright Center of Innovation. Support for acquisition of the XPS system was provided by the National Science Foundation under NSF-DMR grant 0114098.

## Supporting material

The online version of this article contains additional supporting material.

Please visit DOI: 10.1016/j.jcat.2007.10.005.

## References

[1] L.G. Tejuca, J.L.G. Fierro, J.M. Tascon, Adv. Catal. 36 (1989) 237.
[2] M.A. Pena, J.L.G. Fierro, Chem. Rev. 101 (2001) 1981.
[3] L.G. Tejuca, J.L.G. Fierro (Eds.), Properties and Applications of Perovskite-Type Oxides, Marcel Dekker, New York, 1993.
[4] H.J.M. Bouwmeester, H. Kruidhof, A.J. Burggraaf, Solid State Ionics 72 (1994) 185.
[5] J.F. Vente, S. McIntosh, W.G. Haije, H.J.M. Bouwmeester, J. Electrochem. Soc. 10 (2006) 581.
[6] Y. Zeng, Y.S. Lin, S.L. Swartz, J. Membrane Sci. 150 (1998) 87.
[7] F.T. Akin, Y.S. Lin, J. Membrane Sci. 209 (2002) 457.
[8] R.M. Ormerod, Chem. Soc. Rev. 32 (2003) 17.
[9] B.C.H. Steele, Solid State Ionics 94 (1997) 239.
[10] S.B. Adler, Solid State Ionics 111 (1998) 125.
[11] S.B. Adler, Solid State Ionics 135 (2000) 603.
[12] S.B. Adler, Chem. Rev. 104 (2004) 4791.
[13] S.B. Adler, J.A. Lane, B.C.H. Steele, J. Electrochem. Soc. 143 (1996) 3554.
[14] V.C. Corberan, L.G. Tejuca, A.T. Bell, J. Mater. Sci. 24 (1989) 4437.
[15] M.B. Badlani, I.E. Wachs, Catal. Lett. 75 (2001) 137.
[16] G. Busca, Catal. Today 27 (1996) 457.
[17] J.C. Lavalley, Catal. Today 27 (1996) 377.
[18] T. Nitadori, T. Ichiki, M. Misono, Bull. Chem. Soc. Jpn. 61 (1988) 621.
[19] N.A. Merino, B.P. Barbero, P. Ruiz, L.E. Cadus, J. Catal. 240 (2006) 245.
[20] T. Seiyama, N. Yamazoe, K. Eguchi, Ind. Eng. Chem. Prod. Res. Dev. 24 (1985) 19.
[21] T. Shimizu, Appl. Catal. 28 (1986) 81.
[22] T. Nitadori, M. Misono, J. Catal. 93 (1985) 459.
[23] N.A. Merino, B.P. Barbero, C. Cellier, J.A. Gamboa, L.E. Cadus, Catal. Lett. 113 (2007) 130.
[24] Y. Teraoka, H.-M. Zhang, N. Yamazoe, Chem. Lett. (1985) 1367.
[25] J.N. Kuhn, U.S. Ozkan, Catal. Lett. (2007), submitted for publication.
[26] L. Bedel, A.-C. Roger, C. Estournes, A. Kiennemann, Catal. Today 85 (2003) 207.
[27] L. Bedel, A.-C. Roger, J.-L. Rehspringer, Y. Zimmerman, A. Kiennemann, J. Catal. 235 (2005) 279.
[28] J.F. Moulder, W.F. Stickle, P.E. Sobol, K.D. Bomben, Handbook of X-Ray Photoelectron Spectroscopy, second ed., Perkin–Elmer, Eden Prairie, MN, 1992.
[29] L.J. Burcham, L.E. Briand, I.E. Wachs, Langmuir 17 (2001) 6164.
[30] L.J. Burcham, L.E. Briand, I.E. Wachs, Langmuir 17 (2001) 6175.
[31] M. Machkova, N. Brashkova, P. Ivanov, J.B. Carda, V. Kozhukharov, Appl. Surf. Sci. 119 (1997) 127.
[32] N. Yamazoe, Y. Teraoka, T. Seiyama, Chem. Lett. (1981) 1767.
[33] J.L.G. Fierro, Catal. Lett. 22 (1993) 67.
[34] I. Rodriguez-Ramos, A. Guerrero-Ruiz, M.L. Rojas, J.L.G. Fierro, Appl. Catal. 68 (1991) 217.
[35] H.R. Aghabozorg, B.H. Sakakini, A.J. Roberts, J.C. Vickerman, W.R. Flavell, Catal. Lett. 39 (1996) 97.
[36] J. Choisnet, N. Abadzhieva, P. Stefanov, D. Klissurski, J.M. Bassat, V. Rives, L. Minchev, J. Chem. Soc. Faraday Trans. 90 (1994) 1987.
[37] K.S. De, M.R. Balasubramanian, J. Catal. 81 (1983) 482.
[38] W. Wang, H. Zhang, G. Lin, Z. Xiong, Appl. Catal. B Environ. 24 (2000) 219.
[39] K.S. Song, H.X. Cui, S.D. Kim, S.K. Kang, Catal. Today 47 (1999) 155.
[40] S. Kaliaguine, A. Van Neste, V. Szabo, J.E. Gallot, M. Bassir, R. Muzychuk, Appl. Catal. A Gen. 209 (2001) 345.
[41] S.P. Scott, D. Mantzavinos, A. Hartley, M. Sahibzada, I.S. Metcalfe, Solid State Ionics 152–153 (2002) 777.
[42] A. Hartley, M. Sahibzada, M. Weston, I.S. Metcalfe, D. Mantzavinos, Catal. Today 55 (2000) 197.
[43] D. Ferri, L. Forni, Appl. Catal. A Gen. 16 (1998) 119.
[44] S. Royer, H. Alamdari, D. Duprez, S. Kaliaguine, Appl. Catal. B Environ. 58 (2005) 272.
[45] M.H.R. Lankhorst, J.E. ten Elshof, J. Solid State Chem. 130 (1997) 302.
[46] L.W. Tai, M.M. Nasrallah, H.U. Anderson, D.M. Sparlin, S.R. Sehlin, Solid State Ionics 76 (1995) 259.
[47] L.W. Tai, M.M. Nasrallah, H.U. Anderson, D.M. Sparlin, S.R. Sehlin, Solid State Ionics 76 (1995) 273.
[48] P.M. Raccah, J.B. Goodenough, J. Appl. Phys. 39 (1968) 1209.
[49] P.M. Raccah, J.B. Goodenough, Phys. Rev. 155 (1967) 932.
[50] S. Mathi Jaya, R. Jagadish, R.S. Rao, R. Asokamani, Phys. Rev. B 43 (1991) 13274.
[51] V.G. Bhide, D.S. Rajoria, C.N.R. Rao, G.R. Rao, V.G. Jadhao, Phys. Rev. B 12 (1975) 2832.
[52] P. Ganguly, P.S.A. Kumar, P.N. Santhosh, I.S. Mulla, J. Phys. Condens. Matter 6 (1994) 533.
[53] M.A. Senaris-Rodriguez, J.B. Goodenough, J. Solid State Chem. 118 (1995) 323.
[54] H. Takahashi, F. Munakata, M. Yamanaka, Phys. Rev. B 57 (1998) 15211.
[55] J. Mizusaki, J. Tabuchi, T. Matsuura, H. Yamauchi, K. Fueki, J. Electrochem. Soc. 136 (1989) 2082.
[56] A. Chainani, M. Mathew, D.D. Sarma, Phys. Rev. B 48 (1993) 14818.
[57] T. Ishikawa, S.K. Park, T. Katsufuji, T. Arima, Y. Tokura, Phys. Rev. B 58 (1998) R13326.
[58] J. Mizusaki, T. Sasamoto, W.R. Cannon, H.K. Bowen, J. Am. Ceram. Soc. 66 (1983) 247.